

Local dimensionality and inverse persistence analysis of atmospheric turbulence in the stable boundary layer

Francesco Carbone ^{1,*}, Tommaso Alberti ², Davide Faranda ^{3,4,5}, Daniele Telloni ⁶,
Giuseppe Consolini ² and Luca Sorriso-Valvo ^{7,8}

¹National Research Council, Institute of Atmospheric Pollution Research, C/o University of Calabria, 87036 Rende, Italy

²National Institute for Astrophysics, Institute for Space Astrophysics and Planetology, 00133 Roma, Italy

³Laboratoire des Sciences du Climat et de l'Environnement, CEA Saclay l'Orme des Merisiers, UMR 8212 CEA-CNRS-UVSQ, Université Paris-Saclay & IPSL, 91191, Gif-sur-Yvette, France

⁴London Mathematical Laboratory, London W6 8RH, United Kingdom

⁵LMD/IPSL, Ecole Normale Supérieure, PSL Research University, 75005 Paris, France

⁶National Institute for Astrophysics, Astrophysical Observatory of Torino, 10025 Pino Torinese, Italy

⁷Swedish Institute of Space Physics, Ångström Laboratory, SE-751 21 Uppsala, Sweden

⁸National Research Council, Institute for Plasma Science and Technology, 70126 Bari, Italy



(Received 5 May 2022; accepted 30 November 2022; published 26 December 2022)

The dynamics across different scales in the stable atmospheric boundary layer has been investigated by means of two metrics, based on instantaneous fractal dimensions and grounded in dynamical systems theory. The wind velocity fluctuations obtained from data collected during the Cooperative Atmosphere-Surface Exchange Study–1999 experiment were analyzed to provide a local (in terms of scales) and an instantaneous (in terms of time) description of the fractal properties and predictability of the system. By analyzing the phase-space projections of the continuous turbulent, intermittent, and radiative regimes, a progressive transformation, characterized by the emergence of multiple low-dimensional clusters embedded in a high-dimensional shell and a two-lobe mirror symmetrical structure of the inverse persistence, have been found. The phase space becomes increasingly complex and anisotropic as the turbulent fluctuations become uncorrelated. The phase space is characterized by a three-dimensional structure for the continuous turbulent samples in a range of scales compatible with the inertial subrange, where the phase-space-filling turbulent fluctuations dominate the dynamics, and is low dimensional in the other regimes. Moreover, lower-dimensional structures present a stronger persistence than the higher-dimensional structures. Eventually, all samples recover a three-dimensional structure and higher persistence level at large scales, far from the inertial subrange. The two metrics obtained in the analysis can be considered as proxies for the decorrelation time and the local anisotropy in the turbulent flow.

DOI: [10.1103/PhysRevE.106.064211](https://doi.org/10.1103/PhysRevE.106.064211)

I. INTRODUCTION

The atmospheric boundary layer (ABL) connects the lowest layer of the Earth's atmosphere, the surface layer, to the rest of the troposphere. Its dynamics is fundamental for the transport and exchange of moisture, heat, and momentum with the underlying surface [1–3]. Several studies have examined turbulence in the ABL, showing that its structure can be extremely complex and characterized by multiscale fluctuations [4,5], with turbulent eddies ranging from mesoscales, $L \in [10^2, 10^3]$ m, related to the instability of the mean flow shear, and buoyancy effects [6–11], down to smaller scales, $L \in [10^{-2}, 10^2]$ m, related to the energy-cascade process or fine-scale turbulent bursts [6,10,12–14]. Since the ABL is characterized by continuous thickness modulation over time, all physical quantities related to the flow are subject to large-amplitude fluctuations, due to strong vertical mixing [15,16]. The nocturnal ABL is characterized by terrain-following

flows and stable thermal stratification, responsible for the formation of a stable boundary layer (SBL) [1,17,18]. The net radiative cooling of the ground surface induces a vertical temperature gradient, associated with heat transfer from the ABL to the terrain surface. This cools down the fluid, with the consequent formation of a stable stratified inversion layer.

Understanding the nature of the statistical properties of turbulence under realistic conditions is essential for technological and environmental applications, as well as for multiple experiments [9,19–21]. Numerical simulations [22–25] have been performed to investigate the characteristics of turbulence in the SBL. However, disentangling the scale-dependent features of the flow (i.e., “local” properties) remains a challenging task. In particular, one of the fundamental requirements for developing a comprehensive theoretical framework of the SBL dynamics is to identify a scale-dependent dynamical transition, namely a clear cutoff threshold in the superposition of the fast and slow dynamics of the nonlinear and nonstationary SBL turbulent flow.

Due to their complexity, the analysis of these systems has been focused on features shared by a large class of

*francesco.carbone@cnr.it

phenomena, regardless of the details of their fine structure. In fact, the ABL can be described as a chaotic dynamical system displaying recurrent large-scale configurations [26–30]. Recently, such configurations have been investigated using an approach described by two metrics related to the local dimension and to the local persistence in the phase space (PS) [31,32]. Here such concepts have been applied to the different dynamical regimes of the nocturnal SBL, observed during the Cooperative Atmosphere-Surface Exchange Study–1999 (CASES-99) experiment [9,33–37], with particular focus on understanding the different turbulent behaviors observed in the SBL. Following the classical Kolmogorov description of turbulent fluctuations [38], the two dynamical metrics have been used to characterize the scale-by-scale dynamics over a wide range of scales, spanning from the inertial subrange, where the dynamics are characterized by the so-called energy cascade, up to larger scales, where the energy injection in the cascade occurs. Our results show the existence of a low-dimensional dynamics embedded in a high-dimensional shell. As we will see, while the former is characterized by a three-dimensional structure across the inertial subrange, the latter presents higher-dimensional structures with an increased level of persistence.

II. COOPERATIVE ATMOSPHERE-SURFACE EXCHANGE STUDY–1999

All experimental samples used in this work were collected during the period from 10/01/1999 to 10/31/1999 in Kansas, USA (37.6°N, 96.7°E), on a homogeneous, flat area, making it an ideal site for investigating the atmospheric SBL. According to the Wichita National Weather Service and Argonne Boundary Layer Experiment, nights in October tend to be characterized by clear skies and light near-surface flow, thus contributing to SBL development [33]. The measurements are collected by a cluster of probes consisting of a central meteorological tower and six satellite stations located within a 600-m diameter to resolve the turbulence and the mean flow. The probes are three-dimensional (3D) sonic anemometers and temperature sensors, located at seven different heights above the surface for the central tower and at fixed height of 5 m for the satellite towers [33]. All measurements refer to the stationary regime observed within 00:00:00 → 06:00:00 in local standard time (LST). In this study, we used high-frequency observations (with sampling time $\Delta t = 0.05$ s), of the three wind velocity components $\mathcal{U}_i(t)$ (where $i \doteq \{u(t), v(t), w(t)\}$) and of the temperature $\mathcal{T}(t)$, collected by the six satellite towers.

In order to characterize the turbulence within the SBL, the nondimensional ratio ζ/L is used as an indicator of the atmospheric stability [39,40], where $L = -\rho C_p T u_*^3 / \kappa g H$ is the Monin-Obukhov length scale (ρ being the density of air at temperature T , C_p the specific heat capacity at constant pressure, u_* the friction velocity, $\kappa \simeq 0.4$ the Von Kármán constant, and H the surface turbulent heat flux) and ζ is the height above the ground or in terms of the Richardson number Ri [40–42]. However, it should be noted that accurately estimating the atmospheric stability is still considered a challenging task [43–45]. Here the SBL behavior is defined according to the dynamical stability indicator Π [8,46],

based on a set of simplified model equations for the pressure gradient and isothermal net radiation. In particular, $\Pi \geq 1$ represents nonintermittent behavior, while $\Pi < 1$ represents the intermittent cases.

The CASES-99 samples used in this work can be classified into three main groups and one transient category, according to the Π classification [47]: (i) radiative nights [low energy transport through the atmosphere by the turbulence, see Fig. 1 (top panels)]; (ii) continuous turbulent nights (large conductive heat flux H due to strong radiative surface cooling, Q_{net} , in combination with strong turbulent mixing u_* , see Fig. 1 (middle panels)); and (iii) intermittent nights [irregular repetition of short turbulent bursts with different amplitude generated by local shear effects, Fig. 1 (bottom panels)]. The relevant values of friction velocity u_* , conductive heat flux from the Earth’s surface to the atmosphere H , net radiation Q_{net} , and latent heat fluxes $L_v E$, are listed in Table I. All samples that present mixed properties of the three main groups (e.g., collapse of turbulence with strong variations or modulations in u_* and H) are tagged as transient.

Figure 1 shows the velocity component $\mathcal{U}_1(t)$ and the associated temperature $\mathcal{T}(t)$ for three 1-h subsamples (00:00:00 → 01:00:00 LST), 10/14/1999, 10/15/1999, and 10/18/1999, depicting the three distinct regimes of the SBL: radiative, continuous turbulent, and intermittent, respectively. The Taylor’s frozen hypothesis [1,48] is verified for all data ($T_i \approx 20\%$).

As customary in turbulence studies, the nondimensional power spectral density (PSD) $S_{\mathcal{U}_i}$ for a 2-h subset extracted from sample 10/15/1999 in the continuous turbulent regime (00:00:00 → 02:00:00 LST) is shown in Fig. 2, with the associated Von Kármán spectrum [49,50] superimposed (solid line):

$$\frac{f S_{\mathcal{U}_1}(f)}{\sigma_{\mathcal{U}_1}^2} = \frac{4f_L}{(1 + 70.8f_L^2)^{5/6}}, \quad (1)$$

$$\frac{f S_{\mathcal{U}_{2,3}}(f)}{\sigma_{\mathcal{U}_{2,3}}^2} = \frac{4f_L(1 + 755.2f_L^2)}{(1 + 283.2f_L^2)^{11/6}}, \quad (2)$$

where $f_L = f L_{\mathcal{U}_i} \langle \mathcal{U}_i \rangle^{-1}$ represents the nondimensional frequency; $L_{\mathcal{U}_i}$ is the turbulence integral length scale in the longitudinal, lateral, and vertical directions; and $\sigma_{\mathcal{U}_i}^2$ is the variance of the i th velocity component. The small differences in the range of f_L are due to the slightly different $\langle \mathcal{U}_i \rangle$ and $L_{\mathcal{U}_i}$, which are both sample dependent. In terms of similarity theory [51], a spectral relation (experiments indicating an energy cascade valid in the inertial subrange for $f_L > 0.2$ [50,52], with no information on its upper limit) takes the form $f S_{\mathcal{U}_i}(f) \sigma_{\mathcal{U}_i}^{-2} \sim f^{-2/3}$ [38,53,54], which is plotted for comparison as a dashed line in all panels of Fig. 2.

III. SCALE-DEPENDENT PROPERTIES OF THE STABLE BOUNDARY LAYER: INSTANTANEOUS AND LOCAL DYNAMICS

A. Velocity fluctuations and large-scale decorrelation

Following the K41 phenomenology [38], multiscale analysis has been performed on the classical field increments at scale ℓ , defined as $\delta \mathcal{U}_i(\ell) = \mathcal{U}_i(t + \ell) - \mathcal{U}_i(t)$ [55–59]. For

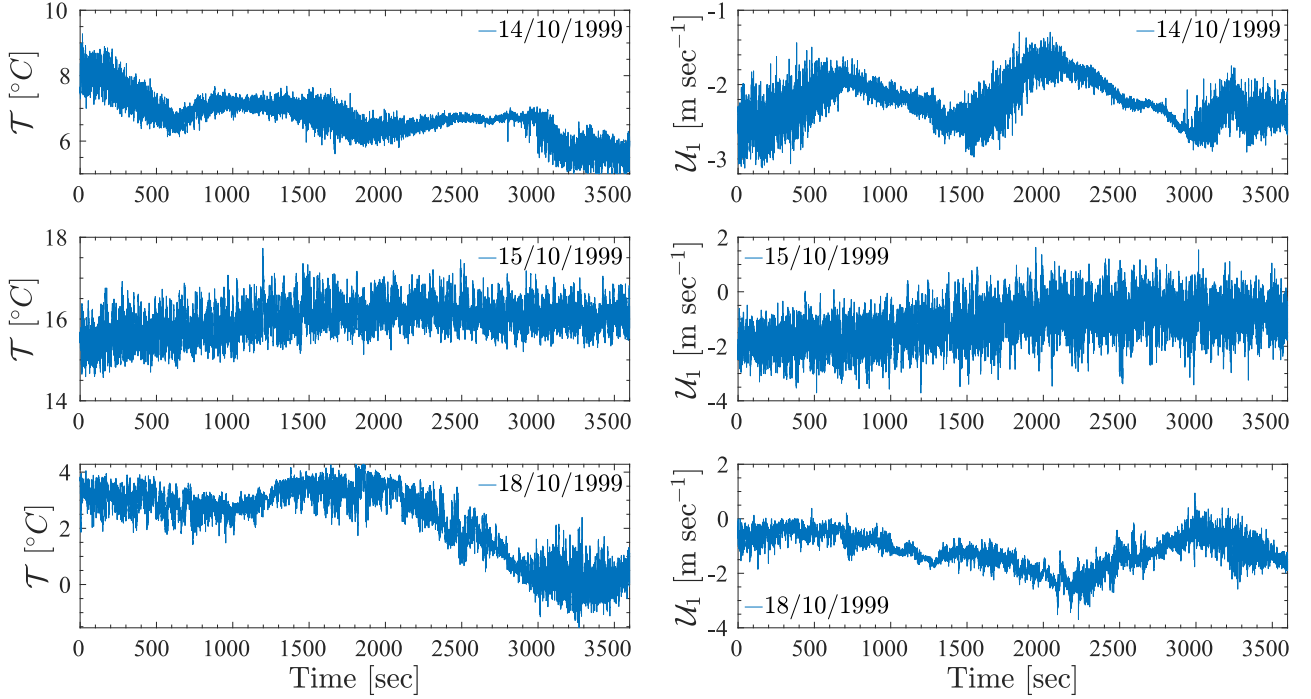


FIG. 1. Left column: Temporal evolution of a 1-h subset of the temperature $\mathcal{T}(t)$ for the three different regimes observed for the SBL: radiative (10/14/1999, upper panel), continuous turbulent (10/15/1999, center panel), and intermittent (10/18/1999, lower panel); all samples are relative to 00:00:00 \rightarrow 01:00:00 in local standard time. Right column: temporal evolution of a 1-h subset, for the same time window, of the first velocity component $\mathcal{U}_1(t)$ observed for the same three SBL regimes. Both temperature and velocity components $\mathcal{U}_1(t)$ were recorded at station I.

fully developed, homogeneous, isotropic turbulence in an infinite medium, the K41 theory assumes that the energy (or information) transfer is constant (in a statistical sense) over a range of scales enclosed in the so-called inertial subrange [38,60,61]. However, the scale-to-scale dynamics is actually far from being uniform, since the breakdown of self-similarity produces the well-known scale variation of the PDFs due to small-scale intermittency [62–65]. As the scale ℓ increases, local correlations are lost, and the probability density function of the velocity fluctuations becomes nearly Gaussian, according to the central limit theorem [66].

TABLE I. Classification of CASES-99 data used in this study, based on turbulent heat flux observations, taken from Ref. [47]: friction velocity [u_* (m s $^{-1}$)], conductive heat flux from the Earth’s surface to the atmosphere [surface turbulent heat flux H (W m $^{-2}$)], net radiation [Q_{net} (W m $^{-2}$)], latent heat fluxes [$L_v E$ (W m $^{-2}$)], and the turbulence intensity as a percentage $T_i\%$ [1,48]. All samples refer to the nighttime period between 00:00:00 and 06:00:00 LST.

Date	Group	u_*	H	Q_{net}	$L_v E$	$T_i\%$
10/13/1999	Transient	0.199	−17.5	−62.5	−1.8	16
10/14/1999	Radiative	0.031	−1.4	−62.8	−0.3	27
10/15/1999	Turbulent	0.494	−45.6	−73.9	5.7	21
10/17/1999	Turbulent	0.594	−5.7	−31.2	12.5	25
10/18/1999	Intermittent	0.094	−4.1	−55.6	2.9	22
10/19/1999	Radiative	0.033	−1.1	−57.6	0.4	23
10/20/1999	Intermittent	0.070	−5.7	−61.9	0.1	22
10/21/1999	Transient	0.115	−14.3	−63.2	−0.2	26

The maximum scale in the analysis has been selected as the scale at which the kurtosis reaches its Gaussian value, $K_\ell(\delta\mathcal{U}_i) \equiv \mu_{\delta\mathcal{U}_i}^{(4)} \sigma_{\delta\mathcal{U}_i}^{-4} = 3$ [$\mu_{\delta\mathcal{U}_i}^{(j)}$ being the j th-order moment of the fluctuation $\delta\mathcal{U}_i$]. The value of $K_\ell(\delta\mathcal{U}_i)$ plays an important role in the classical description of homogeneous, isotropic turbulence. Indeed, a larger $K(\delta\mathcal{U}_i)$ is related to local correlations existing in limited spatial regions, due to structures accumulating at smaller scales that produce non-Gaussian statistics. $K_\ell(\delta\mathcal{U}_i)^{-1}$ represents a heuristic estimate of the order of the fractional space filling factor. The left panel of Fig. 3 shows the scaling of $K_\ell(\delta\mathcal{U}_i)$ for the three velocity components of sample on 10/15/1999, in the range of scales $\ell \in [10, 5000]$ s, along with the associated Gaussian limit value (horizontal dashed line). Fluctuations of the $\delta\mathcal{U}_{1,2}$ components become uncorrelated at $\ell_1 = 3650$ s and $\ell_2 = 5500$ s, respectively. The right panel of Fig. 3 shows the large-scale ($\ell_{K=3}$) PDFs $P(\delta\mathcal{U}_{1,2})$ for all samples, estimated after the usual standardization $\delta\mathcal{U}_i = [\delta\mathcal{U}_i - \mu_{\delta\mathcal{U}_i}^{(1)}] \sigma_{\delta\mathcal{U}_i}^{-1}$ (i.e., subtracting the mean value of the fluctuations and dividing by the standard deviation), with superimposed the corresponding zero-mean, unit-variance normal distribution (dashed line) superimposed. Heavy-tailed distributions are observed at all scales ℓ for $P(\delta\mathcal{U}_3)$. However, it should be pointed out that a fully developed phenomenology does not exist for all the dynamic regimes presented here. Therefore, the largest scale of interest has been defined by using an average scale $\langle \ell_3 \rangle$. As illustrated in the center panel of Fig. 3, fluctuations become uncorrelated, with large-scale kurtosis $K_\ell(\delta\mathcal{U}_i) \approx 3$ ($i = 1, 2$), in the (sample-dependent) range of scale $\ell_3 \equiv \ell_{K=3} \in [0.3, 2.2]$ h, with average scale $\langle \ell_3 \rangle \approx 3400$ s plotted as a

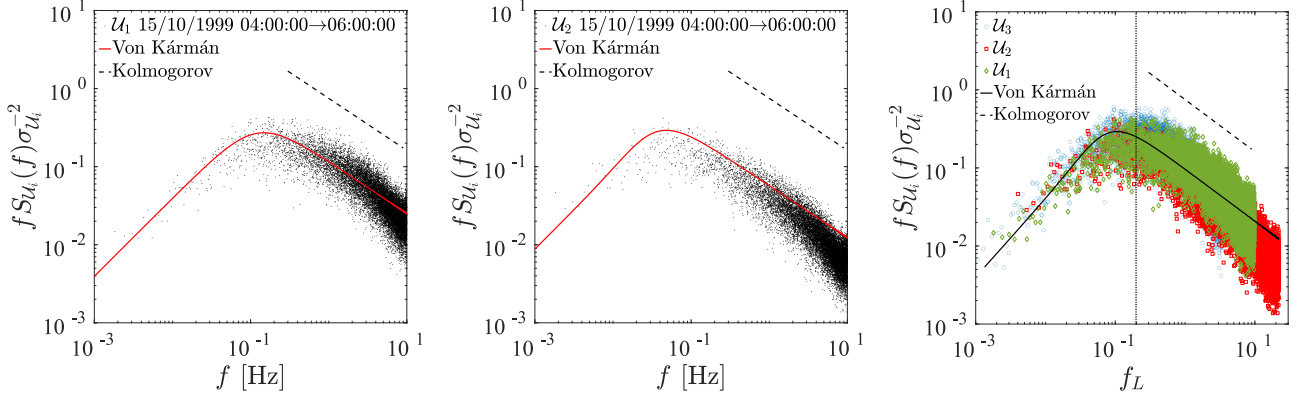


FIG. 2. Left panel: Nondimensional power spectral density (PSD) of the velocity component $\delta\mathcal{U}_1$ as a function of the physical frequency f , with the corresponding Von Kármán spectrum (full line) and the classical Kolmogorov scaling (dashed line) superimposed. Center panel: nondimensional PSD of the velocity component $\delta\mathcal{U}_2$. Right panel: Comparison of the three nondimensional PSD for the three components of the velocity ($\delta\mathcal{U}_{1,2,3}$) as a function of the nondimensional frequency f_L . All PSD overlap, with small differences attributed to the slightly different values of $\langle\mathcal{U}_i\rangle$ and $L_{\mathcal{U}_i}$.

dashed line in the center panel. The component $\delta\mathcal{U}_3$ never reaches the Gaussian value $K_\ell(\delta\mathcal{U}_3) = 3$, regardless of the sample, probably due to the small-scale intermittency of the stratified atmospheric flow [5,16,67–69]. For this reason, it has been excluded from the calculation of the large-scale average. In light of this, a range of scales $\ell \in [2\Delta t, 72000\Delta t]$ ($0.1 \rightarrow 3600$ s) has been selected for the analysis, enclosing both the inertial subrange and the larger scales affected by mean flow instabilities, such as local shear or buoyancy.

B. Scale-dependent dimension and persistence of the phase-space trajectories

The local properties of the different boundary layer regimes are investigated in the dynamical systems framework by applying two metrics obtained by sampling the recurrences of a state of interest $\hat{\mathcal{U}}_\ell = \{\delta\mathcal{U}_1(\ell), \delta\mathcal{U}_2(\ell), \delta\mathcal{U}_3(\ell)\}$ in the PS. For each scale ℓ , a pair of parameters [$\mathcal{D}_\ell(t)$ and $\theta_\ell(t)$] can be obtained, enabling us to investigate the instantaneous

scale-dependent features of the velocity field fluctuations. This method, first proposed in Alberti *et al.* [70], has recently been applied to laboratory experiments on Von Kármán fluids and represents an extension of a previous method based on generalized fractal dimensions [71,72]. The first parameter is the local dimension $\mathcal{D}_\ell(t)$, describing the geometry of the system's trajectory in a region of the PS around $\hat{\mathcal{U}}_\ell$, and it represents a measure of the active number of degrees of freedom. According to its definition, the dimension \mathcal{D} is a standard measure of the geometrical complexity of the PS. For $\mathcal{D} = 3$, the PS is uniformly covered by the fluctuations; for $\mathcal{D} = 2$ the turbulent fluctuations are constrained on a two-dimensional plane and along a one-dimensional line for $\mathcal{D} = 1$. In the latter cases, anisotropy exists in the system, for example when turbulent fluctuations are stronger in certain directions. For all noninteger values of \mathcal{D} , the PS geometry of the turbulent fluctuations is predominantly fractal. The concept of dimension can be extended to a multiscale description. A scale-dependent measure of the geometrical properties of

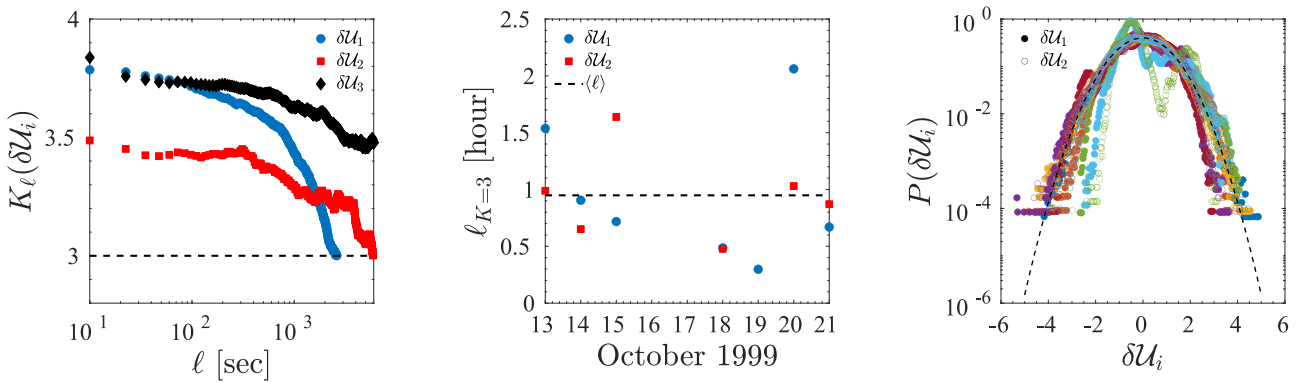


FIG. 3. Left panel: Scale-dependent kurtosis (K_ℓ) for the continuous turbulent sample on 10/15/1999. The components $\delta\mathcal{U}_{1,2}$ become uncorrelated at $\ell_1 = 3650$ s and $\ell_2 = 5500$ s, respectively. For the component $\delta\mathcal{U}_3$, the kurtosis never reaches the Gaussian value $K_\ell = 3$, due to the inherent small-scale intermittency. Center panel: Scale ℓ at which fluctuations $\delta\mathcal{U}_{1,2}$ become uncorrelated ($K_\ell \approx 3$). Data from the day 10/17/1999 were omitted since $K_\ell > 3 \forall \ell$. The horizontal dashed line represents the average, $\langle\ell\rangle = 3400$ s. Right panel: Probability distribution functions $P(\delta\mathcal{U}_{1,2})$ at scale $\ell_{K=3}$ for each sample (except for the sample of 10/17/1999). Full symbols indicate $\delta\mathcal{U}_1$ and empty symbols $\delta\mathcal{U}_2$. A standard zero-mean and unit-variance Normal distribution is superimposed (dashed line).

turbulent fluctuations, $\mathcal{D}_\ell(t)$, can also be introduced, with ℓ indicating a spatial scale. In this case, the topological properties of fluctuations can change scale by scale. If the dimension does not depend of the scale, $\mathcal{D}_\ell(t) = \text{const} \forall \ell$, then the PS has scale-invariant topology. In that case, the turbulent fluctuations are constrained to explore a specific fraction of the PS at all scales. The second parameter used for the description of the SBL is the inverse persistence $\theta_\ell(t)$. This parameter is related to the system's typical residence time in the neighborhoods of \hat{U}_ℓ , which is a measure of how long the system persists in states that closely resemble \hat{U}_ℓ , therefore measuring the clustering of the PS [31,73–75]. The parameter $\theta_\ell(t)$ gives a scale-dependent measure of the characteristic timescale of the turbulent “decorrelation.” For $\theta_\ell \rightarrow 0$, the system persistence is infinite at scale ℓ , indicating that its dynamical state does not change with time. In terms of turbulent fluctuations, the structures at a given scale are destabilized by the nonlinear straining or by other decorrelation effects arising during the turbulent cascade. When $\theta_\ell(t)$ increases, the state \hat{U}_ℓ is rapidly destabilized and varies continuously over time. The turbulent structures are then characterized by fast eddy decorrelation timescales and lower levels of persistence. Based on the analysis of several different dynamical systems, four limiting pairs of parameters $\mathcal{D}_\ell(t)$, $\theta_\ell(t)$ can be identified as follows. (i) For $\mathcal{D} \rightarrow 0$ (lower values of \mathcal{D}) and $\theta = 0$, the system lies in the vicinity of a stable fixed point and is therefore in a highly predictable state. Examples include a flow composed of structures with slow decorrelation time or turbulence suppression due to a large-scale mean flow. (ii) For $\mathcal{D} \rightarrow 0$ and $\theta = 1$, the system lies near a saddle node where two fixed points move toward each other, collide, and mutually annihilate, as for example in systems with shorter decorrelation time where the large-scale mean flow tends to abruptly reconfigure over time. (iii) For $\mathcal{D} \rightarrow \infty$ (higher values of \mathcal{D}) and $\theta \rightarrow 0$, the system is on the edge of the attractor or in a disordered state characterized by multiple minima of the potential. An example is given by flows characterized by a large-scale forcing acting as an energy source for faster time-evolving turbulent structures. (iv) $\mathcal{D} \rightarrow \infty$ and $\theta = 1$ represent an exotic state of the system that is hardly observed. For each scale, the instantaneous metrics are obtained by sampling the whole PS and searching for recurrences of its various possible configurations (either similar or different configurations). Let ξ be a given state of the PS, and let $g(\xi) = -\log[\text{dist}(\hat{U}_\ell, \xi)]$ be the logarithmic return. By selecting an upper threshold s as the q th quantile of $g(\xi)$, the Freitas-Freitas-Todd theorem modified by Lucarini *et al.* [31] states that the cumulative distribution of exceedence converges to a generalized Pareto-like distribution (GPD):

$$\mathcal{P}(\xi - s) \sim \exp \left[-\theta \frac{g(\xi) - s}{\sigma} \right], \quad (3)$$

where $\mathcal{D} = \sigma^{-1}$ is the instantaneous dimension and $0 \leq \theta \leq 1$ is the inverse persistence [76]. The GPD arises as the asymptotic distribution of recurrences because of the relationship already discovered by Poincaré: In chaotic systems, the probability of getting close to a small set centered around a point ξ of the underlying attractor decreases exponentially with the size of the set. The Poincaré recurrence theorem also motivates the choice of $g(\xi)$ because (i) the negative sign turns

the minima into maxima, for which the GPD was originally devised, and (ii) using a logarithmic weight for the recurrences rewards values close to the chosen point, ξ . The combined effect of (i) and (ii) ensures convergence to the exponential term of the GPD, where the dimension is simply given by the inverse of the scale parameter σ , and thus is directly proportional to the spread of the trajectories within the ball around ξ .

The contours of both $\mathcal{D}_\ell(t)$ and $\theta_\ell(t)$ in the time- ℓ plane are shown in Fig. 4 for three different regimes. In particular, the top row of Fig. 4 depicts the evolution of $\mathcal{D}_\ell(t)$ and $\theta_\ell(t)$ for a continuously turbulent sample (10/15/1999). At all scales, the number of degrees of freedom is approximately $\mathcal{D}_\ell(t) \simeq 3$, reaching larger values only at some specific times and/or scales. This indicates the existence of an external forcing, highlighted by the magenta vertical stripes (see Fig. 4, top row, left panel). The same behavior is observed for the sample recorded on 10/17/1999 (not shown). The uniformity of \mathcal{D}_ℓ over the entire range of scales ℓ can be also clearly seen by looking at the PDF $P(\mathcal{D}_\ell)$, shown in Fig. 5, top row, left panel, where the scale ℓ is color coded. Indeed, all distributions collapse on the same right-tailed PDF with a characteristic peak at $\mathcal{D}_\ell \simeq 3$, showing that the PDFs are independent of the scale.

The inverse persistence $\theta_\ell(t)$ presents a rapid variation with ℓ , with steady evolution over time (Fig. 4, top row, right panel). Two distinct sectors can be identified, with a cutoff at $\ell \approx 1$ s: one containing the small scales of the inertial subrange, $2\Delta t \leq \ell \leq 1$ s, and the other composed of large-scale fluctuations or energy injection sources in the range of scales $1 < \ell \leq \langle \ell_3 \rangle$ s. The first sector is characterized by a rapid decrease from $\theta_\ell \simeq 0.94$ at $\ell = 2\Delta t$ to $\theta_\ell = 0.69$ at $\theta_\ell = \langle \ell_3 \rangle$, indicating unstable behavior of this portion of the scale-dependent PS. In other words, the PS starts to develop unstable orbits with the formation of strange attractors [77,78]. The second range of scales presents an almost homogeneous distribution of θ_ℓ , up to $\ell \geq 200$ s, where a slight decrease is observed in the average θ_ℓ . Such behavior is also seen in the evolution of the scale-dependent PDF $P(\theta_\ell)$ (Fig. 5, bottom row, left panel). Starting from a narrow PDF peaking at $\theta_\ell = 0.94$ at the smallest scale, the increment of the scale results in the broadening of the PDF, with a peak shifted to smaller θ_ℓ . Finally, for scales in the range $90 < \ell \leq \langle \ell_3 \rangle$ s, all PDFs collapse on the same distribution, with a peak at $\theta_\ell = 0.64$. Despite the difference in the turbulent heat flux H and in latent heat flux $L_v E$, the same behavior is also observed for the second turbulent sample, on 10/17/1999. In fact, both samples exhibit comparable friction velocity u_* (strong turbulent mixing), which characterizes the surface shear, constraining the PS dynamics for both metrics.

A completely different situation is observed for the intermittent sample on 10/18/1999 and for the radiative sample on 10/14/1999 (see Fig. 4, left panels, center and bottom row, respectively). In both cases, the time- ℓ plane of the local dimension \mathcal{D}_ℓ is fragmented in to multiple temporal regions, each characterized by strong variability. Contrary to the continuous turbulent case, here the local dimension presents a complex temporal evolution, strictly connected to the scale under analysis. In particular, the local dimension is continuously “stretched and expanded” with an excursion

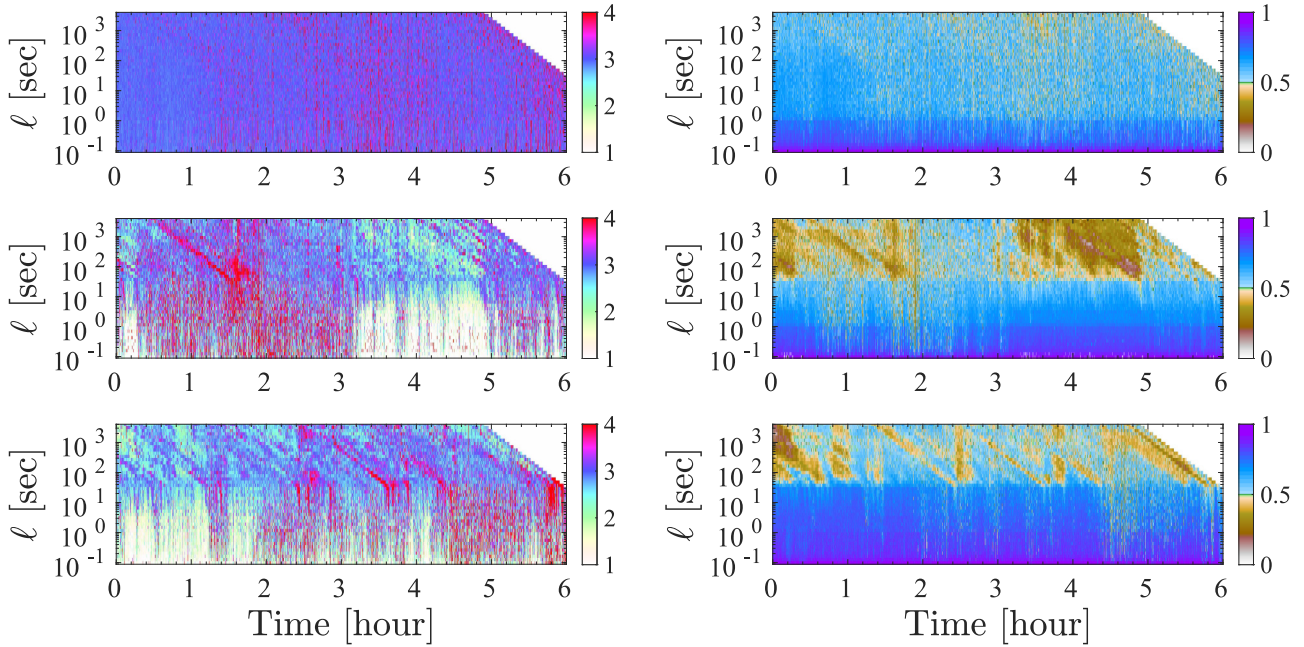


FIG. 4. Local dimension $\mathcal{D}_\ell(t)$ (left column) and dynamical stability index $\theta_\ell(t)$ (right column), obtained from the PS state \hat{U}_ℓ , projected on the plane (Time – ℓ), for the continuous turbulent sample on 10/15/1999 (top row), the intermittent sample on 18/10/1999 (center row), and the radiative sample on 10/14/1999 (bottom row). All values $\mathcal{D}_\ell(t) > 4$ have been set to 4 in order to enhance the readability of the maps. All maps refer to station 1.

enclosed in the range $0.1 \leq \mathcal{D}_\ell \leq 10$, indicating a continuous “local” reorganization of the turbulent fluctuations. As shown in Fig. 5, top row, center and right panels, the main difference among the continuous turbulent and radiative/intermittent samples is the reduction of the PS dimensionality, which highlights a transition from a three-dimensional structure to lower-dimensional ones. Both PDFs are described by similar heavy right tails at large scales but have different shapes at smaller scales. In particular, the intermittent sample presents a stronger reduction of the dimensionality up to $\mathcal{D}_\ell \approx 0.10$ with respect to the radiative samples, which are characterized by a lower bound for the dimensionality, of the order of $\mathcal{D}_\ell \approx 0.60$. In this situation, the exchanges of sensible and latent heat between the surface and the atmosphere is stronger than the turbulent mixing u_* , and the flow is composed of discrete parcels carrying different values of temperature, momentum, and moisture, which can affect the local properties and the dimensionality of the process.

For the inverse persistence θ_ℓ , the time- ℓ plane for both the intermittent and the radiative samples can be divided into three groups of scales, separated by two distinct cutoffs (Fig. 4 center and bottom rows, right panels). The first group consists of all scales $2\Delta t \leq \ell \leq 1$ s, whose boundaries are sharp and clearly observable in the intermittent case (Fig. 4 center row, right panel) and smoother in the radiative case. The second group is composed of all scales $1 < \ell \leq 55$ s. Finally, the third group is composed of scales $55 < \ell \leq \langle \ell_3 \rangle$ s. All scales in the first and second groups are strongly unstable. The PDFs evolve when passing from $\theta_\ell \approx 0.92$ to $\theta_\ell \approx 0.70$ for the first group and from $\theta_\ell \approx 0.95$ to $\theta_\ell \approx 0.8$ for the second group. A secondary peak [less visible in the PDFs $P(\mathcal{D}_\ell)$], located at $\theta_\ell \approx 0.30$ for the intermittent case and $\theta_\ell \approx 0.35$ for the radiative case, is observed. This indicates a bistable distribution

of the fluctuations, so that the PS possesses multiple repelling or attracting points.

Finally, the secondary transition to a more stable dynamics is observed at larger scales, representing the third group. By analyzing the timescale maps, the inverse persistence parameter shows clusters of different size in both time and scale (Fig. 4, center and bottom rows, right panels). The distributions $P(\theta_\ell)$ tend to collapse on a wider distribution, which encompasses a larger range of variation, $0.1 \leq \theta_\ell \leq 0.6$ (see Fig. 5, bottom row, center and right panels), with the core of the distribution peaked at $\theta_\ell \approx 0.35$ for the intermittent case and $\theta_\ell \approx 0.50$ for the radiative case. In particular, the intermittent cases shows a wider PDF than the radiative cases. The latter are characterized by a strong decrease of the left tail of the PDFs, followed by a scale-dependent secondary peak in the range $0.15 \leq \theta_\ell \leq 0.20$, probably due to the different properties among of the various flow parcels.

Figures 6–9 show PS projections of \mathcal{D}_ℓ and θ_ℓ , at three different scales, for the intermittent sample on 10/18/1999 and for the continuous turbulent sample on 10/15/1999, respectively. All maps were constructed from the intersection of all points composing the state vector \hat{U}_ℓ normal to the plane $\{0, 0, 1\}$ (left column), $\{0, 1, 0\}$ (center column), and $\{1, 0, 0\}$ (right column), respectively, taken at $\delta\mathcal{U}_i = 0$. In all cases, a key parameter to discriminates the behavior of $\mathcal{D}_\ell(t)$ and $\theta_\ell(t)$ is the amplitude of the fluctuations. In fact, at all scales, structures with lower dimensionality and persistence are characterized by lower energy levels. As the scale increases, more higher-dimensional and stable regions appear on the edges of the map. For the intermittent sample, at scale $\ell = 0.4$ the inverse persistence [Figs. 6 (top row)] presents an almost isotropic cylindrical structure, extending along the

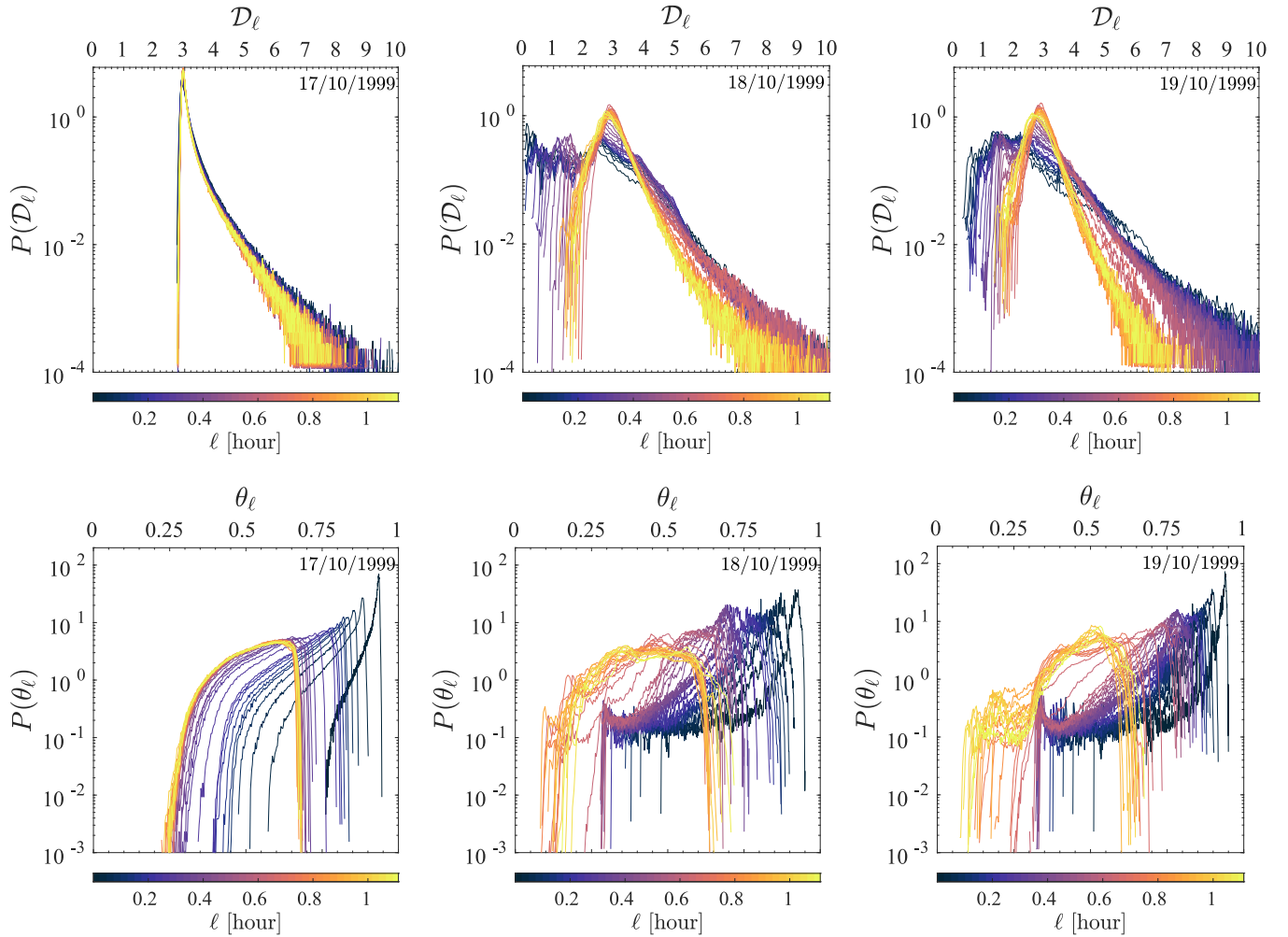


FIG. 5. Probability distribution functions of the local dimensionality \mathcal{D}_ℓ (top row) and inverse persistence parameter θ_ℓ (bottom row) for three distinct regimes: continuous turbulent 10/17/1999, intermittent 10/18/1999, and radiative 10/19/1999, respectively. Each PDF is color coded according to the scale ℓ under analysis.

$\delta\mathcal{U}_3$ component. Such a structure is composed of an unstable internal region $\theta_\ell \approx 0.6$ (plane defined by the components $\delta\mathcal{U}_{1,2}$) contained in a stable region $\theta_\ell \leq 0.45$ (planes $\delta\mathcal{U}_{1,3}$ and $\delta\mathcal{U}_{2,3}$), consistent with the results obtained for the kurtosis. As the scale increases, the stable region tends to extend in the peripheral regions of the plane, and the unstable region tends to concentrate in a structure composed of two distinct lobes, symmetric with respect to a plane perpendicular to the phase space (specular structure). The intersection cuts the plane $\delta\mathcal{U}_{1,2}$ with an angle $\phi \approx 50^\circ$ [Fig. 6 (second row, left panel)]. The symmetric structure is particularly evident for the plane $\hat{\mathcal{U}}_\ell \equiv \{\delta\mathcal{U}_1, 0, \delta\mathcal{U}_3\}$, and $\ell = 600$ s [Fig. 6 (center column, second and third rows)], with a quasisymmetrical reflection along the center line $\delta\mathcal{U}_2 = 0$. Such a “butterfly” structure, observed in the unstable region of the plane, somewhat resembles the two-lobed strange attractor observed in the low-dimensional Galerkin truncation of the Navier-Stokes equations, whose appearance is a consequence of the instability of all the orbits present in the system [78,79]. The same behavior is observed for $\hat{\mathcal{U}}_\ell \equiv \{0, \delta\mathcal{U}_2, \delta\mathcal{U}_3\}$ with the plane along the line $\delta\mathcal{U}_1 = 0$, and also for larger scales (e.g., $\ell = 3600$ s, Fig. 6, center and right panels, bottom row).

Similar structures have been observed for the radiative sample. Both regimes also present the characteristic double-peaked PDFs.

The continuous turbulent sample presents a simpler and rather homogeneous structure of the PS. In fact, at small scales the phase plane presents a spherical structure with an unstable core in the central region [small-amplitude fluctuations, Fig. 8 (top row)]. The map becomes anisotropic and is surrounded by an external shell of stable fluctuations whose thickness increases as the scale exceeds the inertial subrange [large-amplitude fluctuations, Fig. 8 (center row)]. Above the threshold $\ell \approx 2$ s, the thickness of the external stable shell remains almost constant, while the shape of the map becomes stretched and elongated by shrinking along the dimension $\delta\mathcal{U}_3$ up to scales comparable with $\langle \ell_3 \rangle$. An example is shown in the bottom row of Fig. 8, for the scale $\ell \geq 3600$ s, where the map presents an oblate spheroidal structure.

Concerning the dimensionality of the system, a rich and complex structure is observed in the projection of \mathcal{D}_ℓ for the intermittent samples (Fig. 7), where the PS presents a strong dependence on the scale ℓ . In the left column of Fig. 7 is reported the evolution of the PS $\hat{\mathcal{U}}_\ell = \{\delta\mathcal{U}_1, \delta\mathcal{U}_2, 0\}$

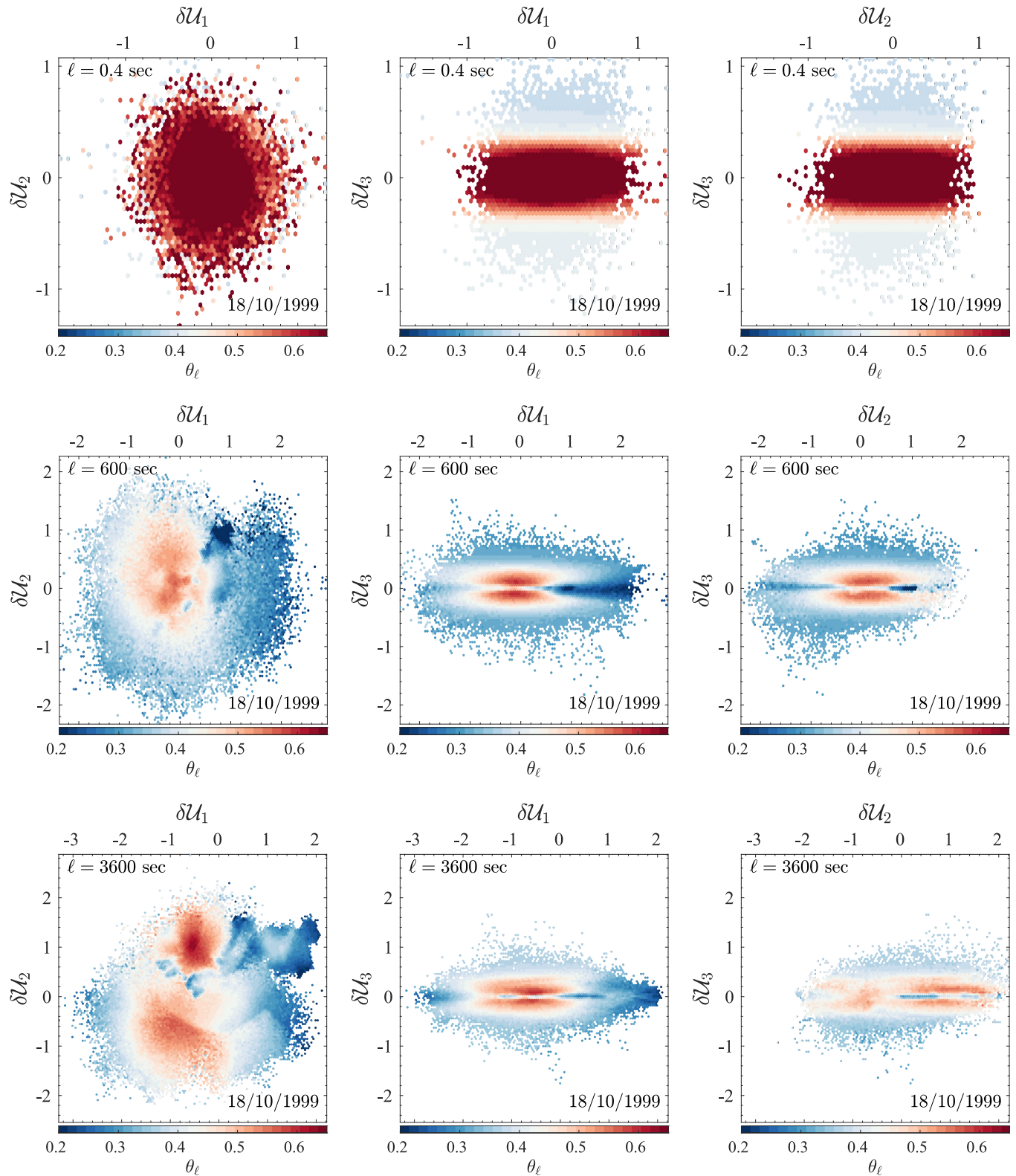


FIG. 6. Poincaré maps for the intermittent sample 10/18/1999 on three different planes (columns) and at three different scales (rows) for the inverse persistence θ_ℓ . The space evolves with the scale from a dense unstable region, extending along the component $\delta\mathcal{U}_3$ and embedded in a more stable region (top row), to a specular symmetric structure with two unstable lobes embedded in a stable region (center and bottom rows). On the plane $\delta\mathcal{U}_{1,2}$, the evolution presents a *disordered* spatial distribution of multiple regions, characterized by both stable and unstable regions respectively (left column).

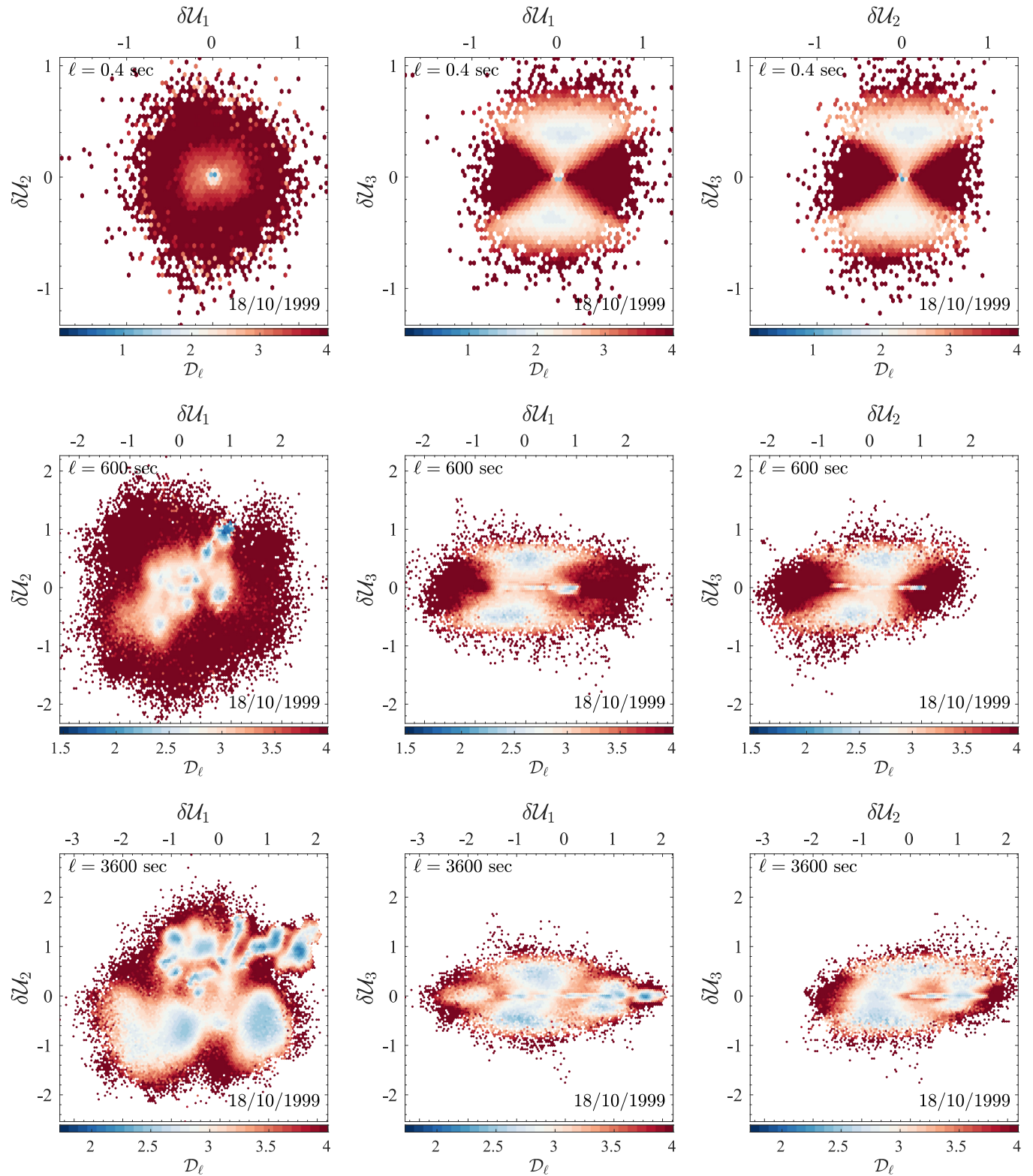


FIG. 7. Poincaré maps for the intermittent sample 10/18/1999 on three different planes (columns) and for three different scales (rows) for the dimensionality D_ℓ . First column: Scale-by-scale emergence of lower-dimensional region in a higher-dimensional background, observed on the plane $\delta\mathcal{U}_{1,2}$. Second column: Transition from a quadrupolar to a specular symmetric structure on the plane $\delta\mathcal{U}_{1,3}$. Third column: Same as previous case in the plane $\delta\mathcal{U}_{2,3}$.

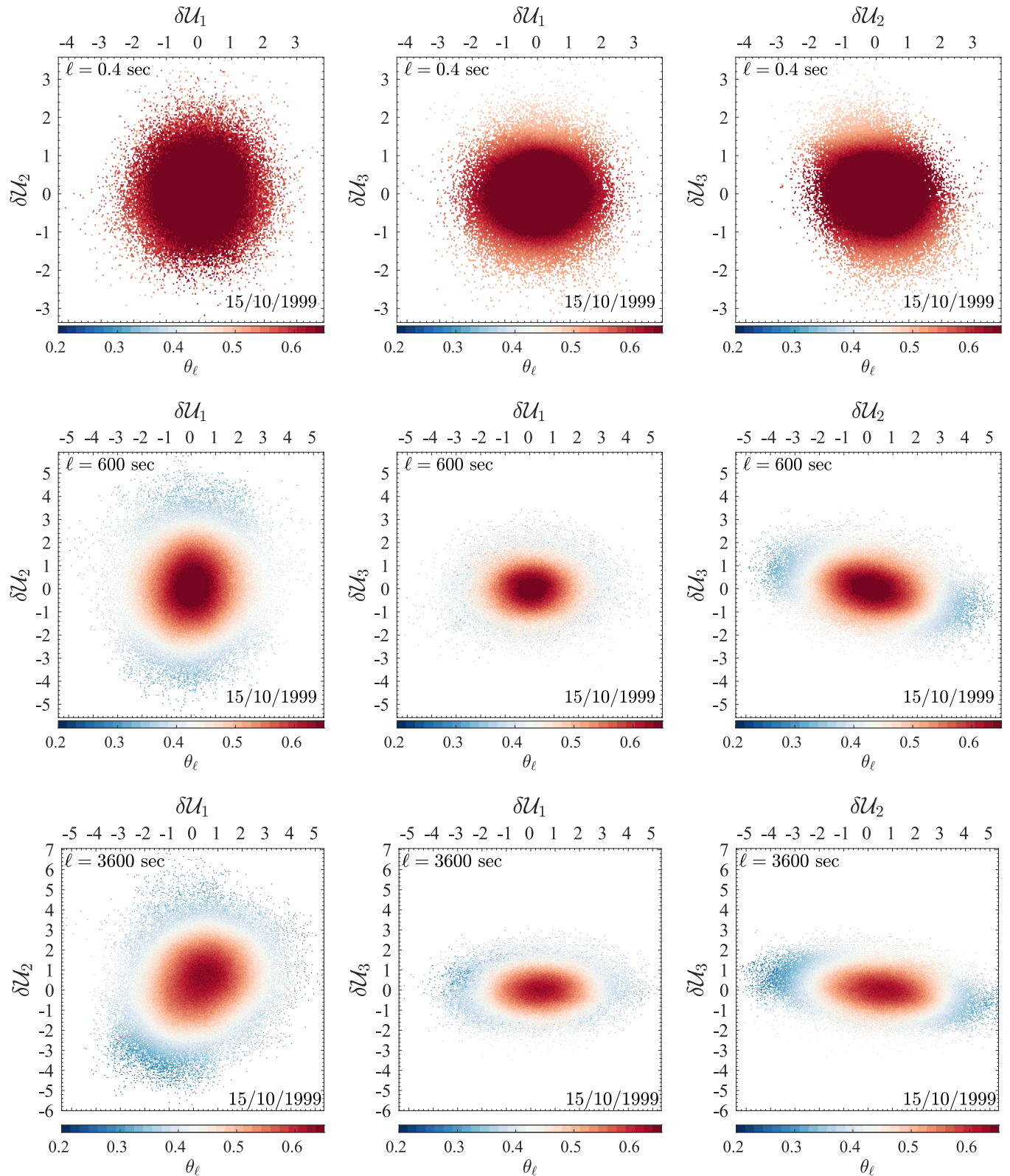


FIG. 8. Poincaré maps for the continuous turbulent sample 10/15/1999 on three different planes (columns) and at three different scales ℓ (rows) for the inverse persistence θ_ℓ . Starting from a fully unstable region, with an almost isotropic shape, in the range of scales comparable with the inertial subrange (top row) the system evolves with the scale ℓ toward a stretched structure, characterized by an unstable region embedded in a stable one of constant thickness (center and bottom rows). The strongly anisotropic structure is particularly evident along the dimension $\delta\mathcal{U}_3$.

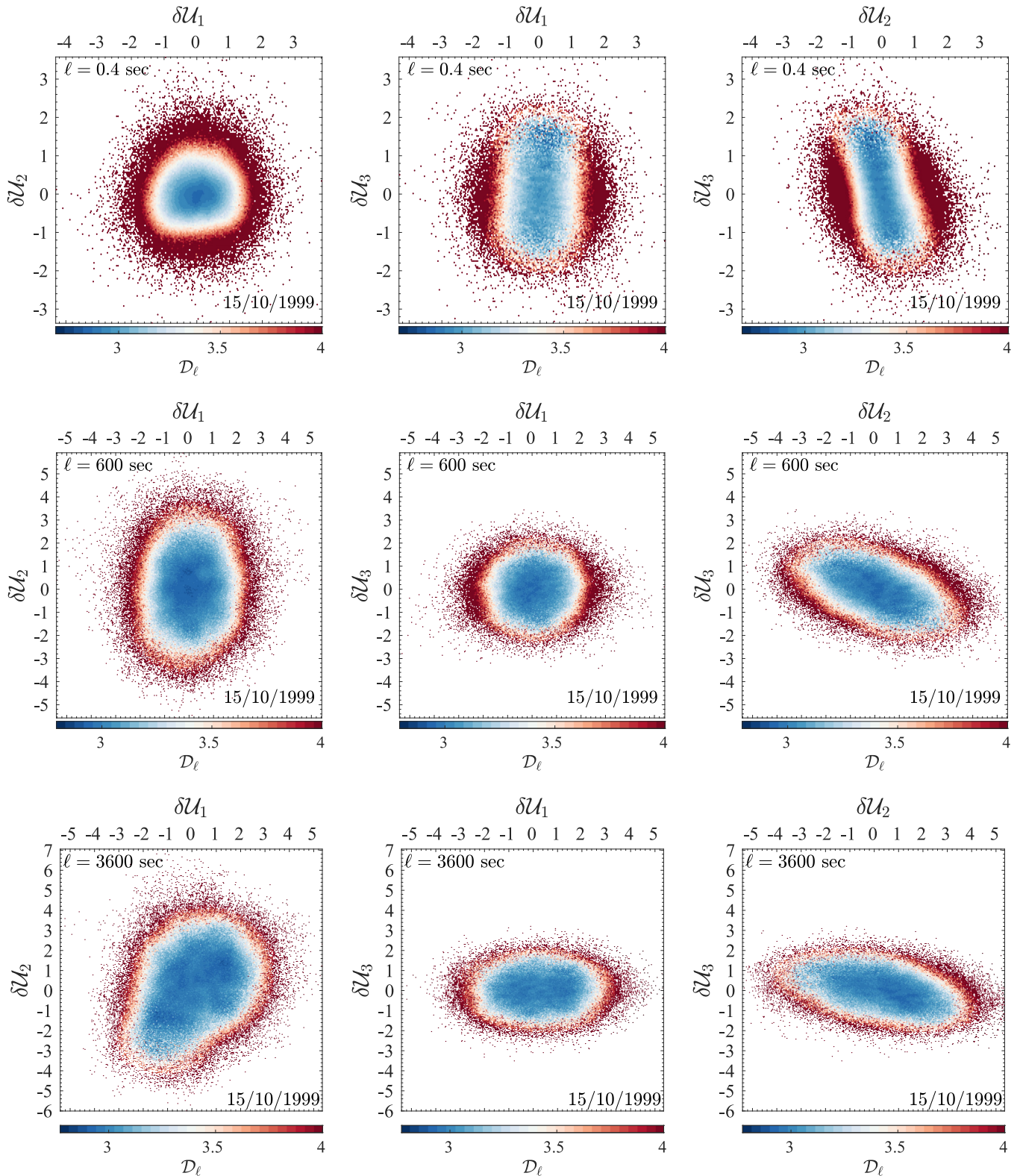


FIG. 9. Poincaré maps for the continuous turbulent sample 10/15/1999 on three different planes (columns) and at three different scales (rows) for the dimensionality D_ℓ . The dimensionality presents a similar structure on all planes composed of a three-dimensional center region surrounded by a higher-dimensional shell for extreme values. An inversion of the anisotropy is observed as the scale increases. For the inertial range (top row), the system is almost isotropic (i.e. spherical in 3D, circular in 2D) on the plane $\delta\mathcal{U}_{1,2}$ and strongly stretched along the dimension $\delta\mathcal{U}_3$ such structure is reverted (center and bottom rows), since the system appear almost isotropic on the plane $\delta\mathcal{U}_{1,3}$ and strongly stretched along the dimension $\delta\mathcal{U}_2$.

as a function of the scale. Starting from an isotropic map composed of a very small spot with $\mathcal{D}_\ell \approx 1$ embedded in a higher-dimensional cluster, the PS undergoes a continuous transformation, characterized by the emergence of multiple clusters of low dimensionality, whose size and number increase with ℓ . The projection on the other two planes, $\hat{\mathcal{U}}_\ell = \{\delta\mathcal{U}_1, 0, \delta\mathcal{U}_3\}$ and $\hat{\mathcal{U}}_\ell = \{0, \delta\mathcal{U}_2, \delta\mathcal{U}_3\}$ [Fig. 7 (center and right columns, respectively)], again presents a stretching along $\delta\mathcal{U}_3$, and a transition from a quadrupolar structure [Fig. 7 (top row, center panel)] to the two-lobed mirror symmetric structure [Fig. 7 (bottom row, center panel)], in the range of scales $2\Delta t \leq \ell \leq 1000$ s. The evolution of the radiative sample follows a similar path, characterized by the emergence of small low-dimensional clusters embedded in a higher-dimensional background and the formation of a mirror symmetric structure (not shown).

The continuous turbulent samples present a simple and uniform structure for \mathcal{D}_ℓ , as illustrated in Fig. 9. In these cases, the PS presents a $\mathcal{D}_\ell = 3$ core in the center of the plane, surrounded by a higher-dimensional shell, whose thickness decreases with the scale. The structure is weakly anisotropic on a single plane that depends on the scale and strongly anisotropic on the other two. For example, at $\ell = 0.4$ s [Fig. 9 (top row)] the structure is weakly anisotropic in the plane $\hat{\mathcal{U}}_\ell = \{\delta\mathcal{U}_1, \delta\mathcal{U}_2, 0\}$ and strongly anisotropic, with a stretched and elongated shape on $\hat{\mathcal{U}}_\ell = \{\delta\mathcal{U}_1, 0, \delta\mathcal{U}_3\}$ and $\hat{\mathcal{U}}_\ell = \{0, \delta\mathcal{U}_2, \delta\mathcal{U}_3\}$. The situation is reversed for larger scales, e.g., $\ell = 600$ s and $\ell = 3600$ s [Fig. 9 (center and bottom rows, respectively)], where the anisotropic structure is observed for the plane $\hat{\mathcal{U}}_\ell = \{\delta\mathcal{U}_1, 0, \delta\mathcal{U}_3\}$ and stretched in the planes $\hat{\mathcal{U}}_\ell = \{\delta\mathcal{U}_1, \delta\mathcal{U}_2, 0\}$ and $\hat{\mathcal{U}}_\ell = \{0, \delta\mathcal{U}_2, \delta\mathcal{U}_3\}$.

To check for spatial dependence of the two indicators, in Fig. 10 we show the temporal average of the two metrics obtained at different satellite stations for all the regimes presented in Table I. For the continuous turbulent sample on 10/15/1999, all stations present the same values of both $\langle \mathcal{D}_\ell \rangle$ and $\langle \theta_\ell \rangle$ [Fig. 10 (first column, left panels, first and second row)]. The local dimensionality shows a constant value $\langle \mathcal{D}_\ell \rangle = 3.1$, indicating a global three-dimensional structure of the PS, with only a weak effect of the large-scale forcing ($\langle \mathcal{D}_\ell \rangle > 3$), which is independent of the station under analysis. Moreover, the same behavior is observed for the inverse persistence parameter: All stations present the same decreasing behavior. The two sectors observed in the dynamical stability index θ_ℓ for sample 10/15/1999 (Fig. 4 (top row, right panel)) are still evident. The first group is characterized by a rapidly decreasing curve over the range of scales $2\Delta t \leq \ell \leq 1$ s, passing from $\langle \theta_\ell \rangle = 0.9$ to $\langle \theta_\ell \rangle = 0.6$ at $\ell \approx 2$ s. The second cluster has a constant value of the inverse persistence $\langle \theta_\ell \rangle = 0.6$ in the range of scales $2 \leq \ell \leq 1000$ s, with a slow decrease to $\langle \theta_\ell \rangle = 0.55$ at very large scales. The turbulent fluctuations explore the entire three-dimensional PS under the effect of strong mixing.

In the center column of Fig. 10, we show the results obtained for the intermittent sample on 10/18/1999. Interestingly, the local dimensionality presents a different scale-by-scale dependence up to a station-dependent limit scale. In fact, an increasing $\langle \mathcal{D}_\ell \rangle$ is observed for the various stations starting from $\langle \mathcal{D}_\ell \rangle \approx 1.7$ (mixed two-dimensional sheet and tangled wires structures) up to $\langle \mathcal{D}_\ell \rangle \gtrsim 3$ (Fig. 10,

first row, center column, center panel), where the fluctuations cover the entire PS at the scale $\ell \approx 200$ s. However, the path to the three-dimensional structure is not the same but rather strictly dependent on the station. The convergence to a similar trend is retrieved only at large scales $\ell \geq 200$. Such complex behavior could be due to the continuous fragmentation and distortion of the various flow parcels resulting from the competition between thermal- and shear-induced fluctuations, and such competition could create self-organized large-scale structures (approximately of the order of the distance between the various satellite stations) able to “transport” with their motion smaller eddies with different local characteristics [80,81]. Despite the strong variations in the dimensionality, a smoother evolution is observed for $\langle \theta_\ell \rangle$ [Fig. 10 (second row, center column, center panel)]. All stations present the same decreasing trend, within small-amplitude variations, from $\langle \theta_\ell \rangle = 0.90$ at $\ell = 2\Delta t$ to $\langle \theta_\ell \rangle = 0.49$ at large scale (ℓ_3). Moreover, the three sections observed in the time- ℓ plane are still evident: The first section in the range $2\Delta t \leq \ell \leq 100$ s is characterized by a fast decrease; the second cluster in the range $2 \leq \ell \leq 100$ s is characterized by quasicontant behavior; and, finally, a third range for $\ell > 200$ s is characterized by strongly stable fluctuations.

A comparison of $\langle \mathcal{D}_\ell \rangle$ and $\langle \theta_\ell \rangle$ for two different samples of each group is shown in the third and fourth rows of Fig. 10. The two continuous turbulent cases show the same behavior for $\langle \mathcal{D}_\ell \rangle$ and $\langle \theta_\ell \rangle$. Small variations in $\langle \theta_\ell \rangle$ are observed for $\ell > 10$ s, probably due to the different thermal properties of the flow. Similar behavior is observed for the intermittent samples. In terms of mean dimensionality, these both have the characteristic peak at $\ell = 200$ s, with small differences in the intermediate range of scales $4\Delta t \leq \ell \leq 40$ s, while a slight difference in the inverse persistence becomes noticeable for $\ell \geq 20$ s. For the radiative sample (10/14/1999 and 10/19/1999), the discrepancy for both metrics is evident at all scales [Fig. 10 (right column)]. The dimensionality differs already at small scales and reaches its minimum at $\ell \approx 100$ s, after which it increases again. The same trend is observed for the inverse persistence, with the only difference that $\langle \theta_\ell \rangle$ seems to converge to a constant value after $\ell \approx 100$ s. Since the thermal parameters are exactly comparable, with the exception of $L_v E$, the heat flux from the Earth’s surface to the atmosphere potentially affects the local properties of the turbulent fluctuations.

Finally, the transient regime demonstrates mixed behavior with elements common to the other regimes for both \mathcal{D}_ℓ and θ_ℓ , respectively. These include, for example, a constant dimensionality or the variation from $\mathcal{D}_\ell < 3$ to a fully three-dimensional structure $\mathcal{D}_\ell = 3$. This mixed behavior is strictly sample and site dependent.

In classical theory of isotropic, fully developed turbulence [38], the hierarchy of fluctuations at all scales is generated by nonlinear straining effects, giving rise to energy transfer toward smaller scales. The field correlation decay is then attributed to nonlinear interactions among triads of wave vectors, and within this framework, the global energy cascade rate scales as $\epsilon \sim u^3 L^{-1}$, where u is the rms turbulence amplitude and L the energy-containing scale. Similarly, a scale-dependent energy cascade rate can be introduced as $\epsilon_\ell \sim u_\ell^3 \ell^{-1} \sim u_\ell^2 \tau_\ell^{-1}$, where ℓ represents the local scale and τ_ℓ

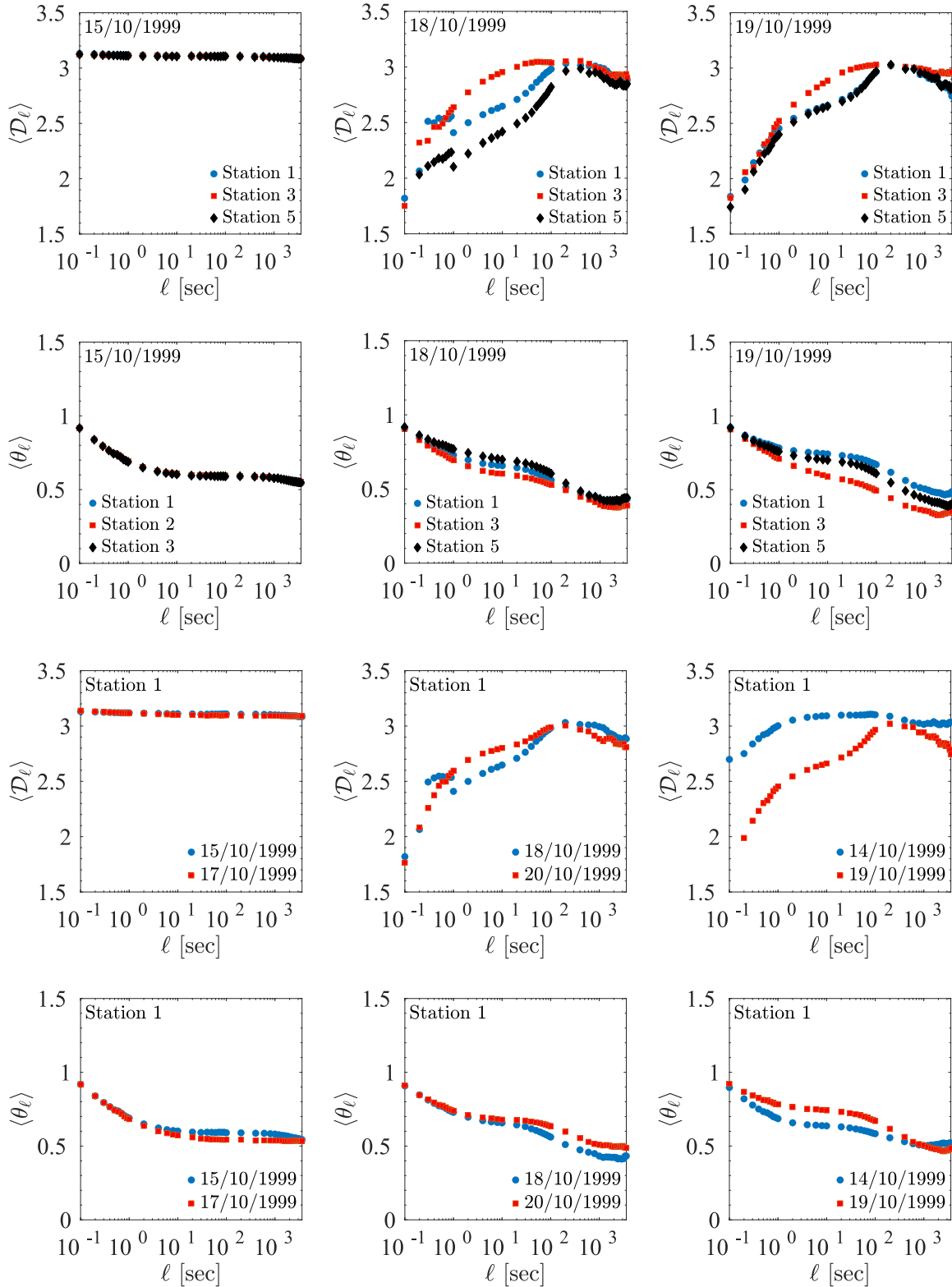


FIG. 10. Temporally averaged local dimensionality $\langle \mathcal{D}_\ell \rangle$ (top row) and inverse persistence parameter $\langle \theta_\ell \rangle$ (second row) measured at three different satellite stations for the continuous turbulent sample on 10/15/1999 (left column), the intermittent sample on 10/18/1999 (center column), and the radiative sample on 10/19/1999 (bottom column). Third and bottom rows: Comparison of the average dimensionality and inverse persistence for two distinct samples of each regime of Table I for a single station.

defines the scale-dependent decorrelation time. In Fourier space, the amplitude of the fluctuations at scale $\ell = 1/k$ is $u_k = \sqrt{kE(k)}$, where $E(k) = \epsilon^{2/3}k^{-5/3}$. As a result, the nonlinear time at scale k is $\tau_k = k^{-1}u_k^{-1}$, indicating that smaller and less energetic scales are characterized by shorter decorrelation time. Such features are robustly captured by the measure, $\langle \theta_\ell \rangle$, which can be considered as a “global proxy” of the cascade properties. Indeed, smaller scales are characterized by lower persistence. With an extremely short decorrelation time, these are continuously affected by the energy flowing from larger scales to the inertial subrange. As the scale ℓ increases, the turbulent structures show increasing persistence due to the slower decorrelation time. This is observed up to a characteristic scale, comparable with the peak of the Von Kármán spectrum (Fig. 2), representing the coherent structures of the flow. At larger scales, the persistence slowly increases, indicating a modification in the PSD exponent or a plateau (depending on the specific sample), separating the fine-scale from large-scale motions (e.g., gravity waves, mesoscale disturbances, or synoptic-scale variability), reaching its maximum (minimum $\langle \theta_\ell \rangle$) at $\ell = 3600$ s. This behavior is robust and only slightly dependent on $\langle \mathcal{D}_\ell \rangle$; indeed, despite the small variations (sample or site specific) observed, the behavior is consistent in each regime analyzed. In fact, whether the fluctuations densely cover the whole three-dimensional space or are constrained to a lower dimensionality, the smaller scales, characterized by fast decorrelation time, are the easiest to destabilize and have lower persistence. Conversely, larger scales (the more energetic coherent structures) have higher persistence. The parameter $\langle \mathcal{D}_\ell \rangle$ is more of a “local proxy” of the flow properties, or, in other words it can be considered as a proxy for the anisotropy of the flow. It seems to be related to the mechanical and thermal properties of the flow due to the atmospheric conditions (e.g., u_* and the heat fluxes).

IV. CONCLUSIONS

In this work the properties of the turbulent stable boundary layer, observed over six nights of the CASES-99 experiment, have been investigated in terms of dynamical systems theory. This was done by sampling the recurrences of a state of interest \mathcal{U}_ℓ , over a fairly wide range of temporal scales ℓ , whose maximum value $\langle \ell_3 \rangle = 3600$ s was empirically determined based on the kurtosis of the fluctuations.

Continuous turbulent samples, where the dynamic is governed by the strong turbulent mixing (comparable friction velocity u_* for both samples), are characterized by constant local dimensions $\mathcal{D}_\ell \approx 3$ at all scales, indicating that the system is able to explore the whole PS, independent of the scale. The inverse persistence θ_ℓ presents a steep variation (indicating a cutoff) that separates the strongly unstable dynamics of the inertial range from the stable dynamics at larger scales (>90 s), where the distributions $P(\theta_\ell)$ collapse on the same shape. The PS projections reveal a weakly anisotropic spherical structure, characterized by a central core with $\mathcal{D}_\ell = 3$ surrounded by a higher-dimensional shell with scale-dependent thickness. Similarly, the inverse persistence θ_ℓ shows a central core of unstable fluctuations and a surrounding external shell of stable fluctuations.

In the intermittent and radiative samples the local dimension \mathcal{D}_ℓ is strongly scale dependent and spatially inhomogeneous, with values in the range $0.1 \leq \mathcal{D}_\ell \leq 3$. This indicates a continuous reorganization of the phase space, and two distinct cutoff scales have been observed in the dynamic. For $\ell \equiv \langle \ell_3 \rangle$ the phase space undergoes a series of continuous transformations characterized by the emergence of multiple clusters of low dimensionality, whose size and number increases with the scale for \mathcal{D}_ℓ . At smaller scales, the distributions $P(\mathcal{D}_\ell)$ peak on a lower-dimensional structure, specifically $\mathcal{D} \approx 1$ for the radiative cases and $\mathcal{D} \leq 1$ for the intermittent samples. The system is therefore not able to explore the entire 3D phase space, but, rather, the dynamics are constrained to a lower-dimensional space at certain times or in certain spatial zones. As the scale increases and exceeds the inertial subrange, the system shifts to a three-dimensional structure, $\mathcal{D} = 3$, with the PDFs convergence on a common shape only being retrieved at larger scales, $\ell \geq 200$ s. The inverse persistence presents a nearly isotropic coaxial cylindrical structure at small scales ($\ell \leq 1$ s), consisting of an unstable internal region with $\theta_\ell \geq 0.55$ and an external stable region with $\theta_\ell \leq 0.45$. As the scale increases, this stable region tends to extend toward the peripheral regions of the plane, while the unstable region tends to concentrate into two distinct symmetric lobes characterized by a specular structure. This transition is accompanied by a shift in the $P(\theta_\ell)$ distributions toward lower θ_ℓ values (higher stability), with the core of the distribution peaking at $\theta_\ell \approx 0.35$ for the intermittent case and at $\theta_\ell \approx 0.50$ for the radiative case. Moreover, the PDFs $P(\mathcal{D}_\ell)$ and $P(\theta_\ell)$ present multiple peaks, probably related to the local competition of thermal and shear-induced fluctuations.

Summarizing, the study of the two metrics \mathcal{D}_ℓ and θ_ℓ presented here enabled us to disentangle the characteristics of the various flow regimes and to identify the presence of sharp changes in the dynamics at specific cutoff temporal scales. Moreover, the two parameters can be considered as proxies for interesting features of the flow. In particular, the inverse persistence θ_ℓ robustly captures the “global properties” of the turbulent cascade by identifying the scale-by-scale variation of the decorrelation time for the turbulent structures embedded in the flow, while the local dimensionality \mathcal{D}_ℓ is mostly related to the “local properties” of the flow and can be considered as a proxy for the anisotropy of the flow. However, further studies are necessary in order to obtain an exhaustive description of the turbulent fluctuations in the framework of the dynamical system theory. The analysis also highlighted the emergence of overlapping space and time multidimensional structures in the dynamics, and that for different regimes thermal effects can be different. Finally, we determined the scale-dependent nature of persistence. The results presented in this work indicate that local dimension and inverse persistence can be useful analysis tools for dynamical systems characterized by scale and spatial variability, such as SBL turbulence.

ACKNOWLEDGMENTS

F.C. acknowledges the contribution received from EU-H2020 program ERA-PLANET through the project “iGOSP” (Grant Agreement 689443), funded under H2020-SC5-15-2015 “Strengthening the European Research Area in the

domain of Earth Observation”; from FET Proactive project “I-Seed,” funded under the Horizon 2020 research and innovation program (Grant Agreement 101017940); and from EU-H2020 project “EuroGEO Showcases: Applications

Powered by Europe” (e-shape) (Grant Agreement 820852), funded under H2020-SC5-2018-2” Strengthening the benefits for Europe of the Global Earth Observation System of Systems (GEOSS)—establishing EuroGEO.”

-
- [1] R. B. Stull, *An Introduction to Boundary Layer Meteorology*, 1st ed., Atmospheric and oceanographic sciences library (Kluwer Academic Publishers, Dordrecht, 1988).
- [2] J. R. Garratt, *The Atmospheric Boundary Layer*, Cambridge Atmospheric and space science series (Cambridge University Press, Cambridge, UK 1992).
- [3] J. Zhang, J. Guo, S. Zhang, and J. Shao, Inertia-gravity wave energy and instability drive turbulence: evidence from a near-global high-resolution radiosonde dataset, *Clim. Dynam.* **58**, 2927 (2022).
- [4] A. M. Obukhov, Some specific features of atmospheric turbulence, *J. Geophys. Res.* **67**, 3011 (1962).
- [5] A. Muschinski, R. G. Frehlich, and B. B. Balsley, Small-scale and large-scale intermittency in the nocturnal boundary layer and the residual layer, *J. Fluid Mech.* **515**, 319 (2004).
- [6] J. C. Wyngaard, Atmospheric turbulence, *Annu. Rev. Fluid Mech.* **24**, 205 (1992).
- [7] G. Amati, R. Benzi, and S. Succi, Extended self-similarity in boundary layer turbulence, *Phys. Rev. E* **55**, 6985 (1997).
- [8] B. J. H. Van de Wiel, R. J. Ronda, A. F. Moene, H. A. R. De Bruin, and A. A. M. Holtslag, Intermittent turbulence and oscillations in the stable boundary layer over land. part i: A bulk model, *J. Atmos. Sci.* **59**, 942 (2002).
- [9] W. Wei, H. S. Zhang, F. G. Schmitt, Y. X. Huang, X. H. Cai, Y. Song, X. Huang, and H. Zhang, Investigation of turbulence behaviour in the stable boundary layer using arbitrary-order hilbert spectra, *Bound.-Layer Meteorol.* **163**, 311 (2017).
- [10] E. Kit, C. M. Hocut, D. Liberzon, and H. J. S. Fernando, Fine-scale turbulent bursts in stable atmospheric boundary layer in complex terrain, *J. Fluid Mech.* **833**, 745 (2017).
- [11] F. Carbone, D. Telloni, A. G. Bruno, I. M. Hedgcock, F. De Simone, F. Sprovieri, L. Sorriso-Valvo, and N. Pirrone, Scaling properties of atmospheric wind speed in mesoscale range, *Atmosphere* **10**, 611 (2019).
- [12] C.-H. Moeng, A large-eddy-simulation model for the study of planetary boundary-layer turbulence, *J. Atmos. Sci.* **41**, 2052 (1984).
- [13] C. Meneveau and K. R. Sreenivasan, The multifractal nature of turbulent energy dissipation, *J. Fluid Mech.* **224**, 429 (1991).
- [14] K. R. Sreenivasan and P. Kailasnath, An update on the intermittency exponent in turbulence, *Phys. Fluids* **5**, 512 (1993).
- [15] C. Rorai, P. D. Mininni, and A. Pouquet, Turbulence comes in bursts in stably stratified flows, *Phys. Rev. E* **89**, 043002 (2014).
- [16] F. Feraco, R. Marino, A. Pumir, L. Primavera, P. D. Mininni, A. Pouquet, and D. Rosenberg, Vertical drafts and mixing in stratified turbulence: Sharp transition with froude number, *Europhys. Lett.* **123**, 44002 (2018).
- [17] L. Mahrt, Stably stratified atmospheric boundary layers, *Annu. Rev. Fluid Mech.* **46**, 23 (2014).
- [18] F. Barbano, L. Brogno, F. Tampieri, and S. Di Sabatino, Interaction between waves and turbulence within the nocturnal boundary layer, *Bound.-Layer Meteorol.* **183**, 35 (2022).
- [19] G. D. Hess, B. B. Hicks, and T. Yamada, The impact of the wangara experiment, *Bound.-Layer Meteorol.* **20**, 135 (1981).
- [20] J. C. Kaimal and J. C. Wyngaard, The kansas and minnesota experiments, *Bound.-Layer Meteorol.* **50**, 31 (1990).
- [21] E. Kit, E. Barami, and H. J. S. Fernando, Structure functions in nocturnal atmospheric boundary layer turbulence, *Phys. Rev. Fluids* **6**, 084605 (2021).
- [22] C.-H. Moeng and P. P. Sullivan, A comparison of shear- and buoyancy-driven planetary boundary layer flows, *J. Atmos. Sci.* **51**, 999 (1994).
- [23] M. Lesieur, *Large-eddy Simulations of Turbulence* (Cambridge University Press, Cambridge, UK 2005).
- [24] R. Stoll, J. A. Gibbs, S. T. Salesky, W. Anderson, and M. Calaf, Large-eddy simulation of the atmospheric boundary layer, *Bound.-Layer Meteorol.* **177**, 541 (2020).
- [25] S. Sukoriansky, E. Kit, E. Zemach, S. Midya, and H. J. S. Fernando, Inertial range skewness of the longitudinal velocity derivative in locally isotropic turbulence, *Phys. Rev. Fluids* **3**, 114605 (2018).
- [26] B. Saltzman, Finite amplitude free convection as an initial value problem-i, *J. Atmos. Sci.* **19**, 329 (1962).
- [27] E. N. Lorenz, Deterministic nonperiodic flow, *J. Atmos. Sci.* **20**, 130 (1963).
- [28] M. Ghil, P. Read, and L. Smith, Geophysical flows as dynamical systems: The influence of Hide’s experiments, *Astron. Geophys.* **51**, 4.28 (2010).
- [29] G. Nevo, N. Vercauteren, A. Kaiser, B. Dubrulle, and D. Faranda, Statistical-mechanical approach to study the hydrodynamic stability of the stably stratified atmospheric boundary layer, *Phys. Rev. Fluids* **2**, 084603 (2017).
- [30] A. Hochman, P. Alpert, T. Harpaz, H. Saaroni, and G. Messori, A new dynamical systems perspective on atmospheric predictability: Eastern mediterranean weather regimes as a case study, *Sci. Adv.* **5**, eaau0936 (2019).
- [31] V. Lucarini, D. Faranda, and J. Wouters, Universal behaviour of extreme value statistics for selected observables of dynamical systems, *J. Stat. Phys.* **147**, 63 (2012).
- [32] D. Faranda, G. Messori, and P. Yiou, Dynamical proxies of north atlantic predictability and extremes, *Sci. Rep.* **7**, 41278 (2017).
- [33] G. S. Poulos, W. Blumen, D. C. Fritts, J. K. Lundquist, J. Sun, S. P. Burns, C. Nappo, R. Banta, R. Newsom, J. Cuxart, E. Terradellas, B. Balsley, and M. Jensen, Cases-99: A comprehensive investigation of the stable nocturnal boundary layer, *Bull. Am. Meteorol. Soc.* **83**, 555 (2002).
- [34] D. C. Fritts, C. Nappo, D. M. Riggan, B. B. Balsley, W. E. Eichinger, and R. K. Newsom, Analysis of ducted motions in the stable nocturnal boundary layer during cases-99, *J. Atmos. Sci.* **60**, 2450 (2003).
- [35] D. Vickers and L. Mahrt, Observations of the cross-wind velocity variance in the stable boundary layer, *Environ. Fluid Mech.* **7**, 55 (2007).

- [36] L. Mahrt and R. Mills, Horizontal diffusion by submeso motions in the stable boundary layer, *Environ. Fluid Mech.* **9**, 443 (2009).
- [37] F. Carbone, T. Alberti, L. Sorriso-Valvo, D. Telloni, F. Sprovieri, and N. Pirrone, Scale-dependent turbulent dynamics and phase-space behavior of the stable atmospheric boundary layer, *Atmosphere* **11**, 428 (2020).
- [38] A. N. Kolmogorov, V. Levin, J. C. R. Hunt, O. M. Phillips, and D. Williams, The local structure of turbulence in incompressible viscous fluid for very large Reynolds numbers, *Proc. R. Soc. London A* **434**, 9 (1991).
- [39] L. Mahrt, Stratified atmospheric boundary layers, *Bound.-Layer Meteorol.* **90**, 375 (1999).
- [40] T. Foken, *Micrometeorology* (Springer, Berlin, 2017), Vol. 308.
- [41] B. Galperin, S. Sukoriansky, and P. S. Anderson, On the critical richardson number in stably stratified turbulence, *Atmos. Sci. Lett.* **8**, 65 (2007).
- [42] Z. Sorbjan, Gradient-based scales and similarity laws in the stable boundary layer, *Quart. J. Roy. Meteorol. Soc.* **136**, 1243 (2010).
- [43] D. Golder, Relations among stability parameters in the surface layer, *Bound.-Layer Meteorol.* **3**, 47 (1972).
- [44] M. Motta, R. J. Barthelmie, and P. Vølund, The influence of non-logarithmic wind speed profiles on potential power output at danish offshore sites, *Wind Energy* **8**, 219 (2005).
- [45] S. Basu, A simple recipe for estimating atmospheric stability solely based on surface-layer wind speed profile, *Wind Energy* **21**, 937 (2018).
- [46] B. J. H. Van de Wiel, A. F. Moene, R. J. Ronda, H. A. R. De Bruin, and A. A. M. Holtslag, Intermittent turbulence and oscillations in the stable boundary layer over land. part ii: A system dynamics approach, *J. Atmos. Sci.* **59**, 2567 (2002).
- [47] B. J. H. Van de Wiel, A. F. Moene, O. K. Hartogensis, H. A. R. De Bruin, and A. A. M. Holtslag, Intermittent turbulence in the stable boundary layer over land. part iii: A classification for observations during cases-99, *J. Atmos. Sci.* **60**, 2509 (2003).
- [48] G. E. Willis and J. W. Deardorff, On the use of taylor's translation hypothesis for diffusion in the mixed layer, *Quart. J. Roy. Meteorol. Soc.* **102**, 817 (1976).
- [49] T. von Kármán, Progress in the statistical theory of turbulence, *Proc. Natl. Acad. Sci. USA* **34**, 530 (1948).
- [50] G. Solari and G. Piccardo, Probabilistic 3-d turbulence modeling for gust buffeting of structures, *Probab. Eng. Mech.* **16**, 73 (2001).
- [51] T. Foken, 50 years of the monin-obukhov similarity theory, *Bound.-Layer Meteorol.* **119**, 431 (2006).
- [52] G. H. Fichtl and G. E. McVehil, Longitudinal and lateral spectra of turbulence in the atmospheric boundary layer at the kennedy space center, *J. Appl. Meteorol. Climatol.* **9**, 51 (1970).
- [53] G. K. Batchelor, *The Theory of Homogeneous Turbulence*, Cambridge Monographs on Mechanics and Applied Mathematics (Cambridge University Press, Cambridge, UK, 1959).
- [54] G. K. Batchelor, The application of the similarity theory of turbulence to atmospheric diffusion, *Quart. J. Roy. Meteorol. Soc.* **76**, 133 (1950).
- [55] U. Frish and G. Parisi, On the singularity structure of fully developed turbulence, in *Turbulence and Predictability in Geophysical Fluid Dynamics and Climate Dynamics*, edited by M. Ghil, R. Benzi, and G. Parisi (North Holland, New York, 1985), pp. 84–88.
- [56] R. Benzi, L. Biferale, G. Paladin, A. Vulpiani, and M. Vergassola, Multifractality in the Statistics of the Velocity Gradients in Turbulence, *Phys. Rev. Lett.* **67**, 2299 (1991).
- [57] R. Benzi, L. Biferale, and G. Parisi, On intermittency in a cascade model for turbulence, *Physica D* **65**, 163 (1993).
- [58] Edited by U. Frisch, *Turbulence: The Legacy of A. N. Kolmogorov* (Cambridge University Press, Cambridge, UK, 1995).
- [59] D. Sornette, *Critical Phenomena in Natural Sciences: Chaos, Fractals, Selforganization, and Disorder: Concepts and Tools*, 2nd ed., Springer Series in Synergetics (Springer, Berlin, 2004).
- [60] R. T. Cerbus and W. I. Goldberg, Information content of turbulence, *Phys. Rev. E* **88**, 053012 (2013).
- [61] C. Granero-Belinchón, S. G. Roux, and N. B. Garnier, Scaling of information in turbulence, *Europhys. Lett.* **115**, 58003 (2016).
- [62] B. Castaing, Y. Gagne, and E. Hopfinger, Velocity probability density functions of high reynolds number turbulence, *Physica D* **46**, 177 (1990).
- [63] I. Mazzitelli and A. S. Lanotte, Active and passive scalar intermittent statistics in turbulent atmospheric convection, *Physica D* **241**, 251 (2012).
- [64] F. Carbone and L. Sorriso-Valvo, Experimental analysis of intermittency in electrohydrodynamic instability, *Eur. Phys. J. E* **37**, 61 (2014).
- [65] F. Carbone, D. Telloni, L. Sorriso-Valvo, G. Zank, L. Zhao, L. Adhikari, and R. Bruno, Statistical analysis of field-aligned alfvénic turbulence and intermittency in fast solar wind, *Universe* **6**, 116 (2020).
- [66] A. A. Townsend, The measurement of double and triple correlation derivatives in isotropic turbulence, *Math. Proc. Camb. Philos. Soc.* **43**, 560 (1947).
- [67] J. C. Kaimal and J. J. Finnigan, *Atmospheric Boundary Layer Flows: Their Structure and Measurement* (Oxford University Press, Oxford, 1994).
- [68] C. R. Chu, M. B. Parlange, G. G. Katul, and J. D. Albertson, Probability density functions of turbulent velocity and temperature in the atmospheric surface layer, *Water Resour. Res.* **32**, 1681 (1996).
- [69] A. C.-L. Chian, R. A. Miranda, D. Koga, M. J. A. Bolzan, F. M. Ramos, and E. L. Rempel, Analysis of phase coherence in fully developed atmospheric turbulence: Amazon forest canopy, *Nonlin. Process. Geophys.* **15**, 567 (2008).
- [70] T. Alberti, D. Faranda, R. V. Donner, T. Caby, V. Carbone, G. Consolini, B. Dubrulle, and S. Vaienti, Small-scale induced large-scale transitions in solar wind magnetic field, *Astrophys. J. Lett.* **914**, L6 (2021).
- [71] T. Alberti, G. Consolini, P. D. Ditlevsen, R. V. Donner, and V. Quattrociochi, Multiscale measures of phase-space trajectories, *Chaos* **30**, 123116 (2020).
- [72] T. Alberti, R. V. Donner, and S. Vannitsem, Multiscale fractal dimension analysis of a reduced order model of coupled ocean-atmosphere dynamics, *Earth Syst. Dynam.* **12**, 837 (2021).
- [73] N. R. Moloney, D. Faranda, and Y. Sato, An overview of the extremal index, *Chaos* **29**, 022101 (2019).
- [74] T. Caby, D. Faranda, G. Mantica, S. Vaienti, and P. Yiou, Generalized dimensions, large deviations and the distribution of rare events, *Physica D* **400**, 132143 (2019).

- [75] G. Messori, N. Harnik, E. Madonna, O. Lachmy, and D. Faranda, A dynamical systems characterization of atmospheric jet regimes, *Earth Syst. Dynam.* **12**, 233 (2021).
- [76] A. C. Moreira Freitas, J. Milhazes Freitas, and M. Todd, The extremal index, hitting time statistics and periodicity, *Advances in Mathematics* **231**, 2626 (2012).
- [77] D. Ruelle and F. Takens, On the nature of turbulence, *Commun. Math. Phys.* **20**, 167 (1971).
- [78] F. Carbone, D. Telsoni, G. Zank, and L. Sorriso-Valvo, Transition to turbulence in a five-mode galerkin truncation of two-dimensional magnetohydrodynamics, *Phys. Rev. E* **104**, 025201 (2021).
- [79] V. Franceschini and C. Tebaldi, Sequences of infinite bifurcations and turbulence in a five-mode truncation of the navier-stokes equations, *J. Stat. Phys.* **21**, 707 (1979).
- [80] T. Sanada and V. Shanmugasundaram, Random sweeping effect in isotropic numerical turbulence, *Phys. Fluids* **4**, 1245 (1992).
- [81] F. Carbone, L. Sorriso-Valvo, C. Versace, G. Strangi, and R. Bartolino, Anisotropy of Spatiotemporal Decorrelation in Electrohydrodynamic Turbulence, *Phys. Rev. Lett.* **106**, 114502 (2011).